Subcycle Conservation Law in Strong-Field Ionization
—— Supplementary Material ——

Yongzhe Ma,[1] Hongcheng Ni,[1,3] Yang Li,[2] Feng He,[2] and Jian Wu[1,3,4]

[1]*State Key Laboratory of Precision Spectroscopy, East China Normal University, Shanghai 200241, China*
[2]*Key Laboratory for Laser Plasmas (Ministry of Education) and School of Physics and Astronomy, Collaborative Innovation Center for IFSA (CICIFSA), Shanghai Jiao Tong University, Shanghai 200240, China*
[3]*Collaborative Innovation Center of Extreme Optics, Shanxi University, Taiyuan, Shanxi 030006, China*
[4]*Chongqing Key Laboratory of Precision Optics, Chongqing Institute of East China Normal University, Chongqing 401121, China*

S1. STRONG-FIELD APPROXIMATION

The subcycle conservation law between angular momentum and energy arises from the infinite-order continuous dynamical symmetry present in the interaction between atoms and circularly or elliptically polarized light pulses. The subcycle conservation law can be characterized using a correlated spectrum of angular momentum and energy (SAME) of photoelectrons produced from strong-field ionization. The SAME in the asymptotic region can be obtained directly from the solutions of the time-dependent Schrödinger equation (TDSE) and the SAME at the tunnel exit can be extracted using the backpropagation method [1–4]. However, these methods fall short of a clear physical picture. To gain deeper insights into the fundamental light-matter interactions, we employ the strong-field approximation (SFA) [5, 6], which is capable of providing closed analytical expressions for the variables of interest. To this end, the transition amplitude between an atomic bound state and the continuum state with photoelectron asymptotic momentum $\boldsymbol{p}$ is written as

$$M_{\boldsymbol{p}} = -i\int_{-\infty}^{+\infty} \langle \psi_{\boldsymbol{p}} | \boldsymbol{r}\cdot\boldsymbol{F}(t) | \psi_i \rangle dt, \tag{S1}$$

where $\boldsymbol{r}$ is the position operator, $\boldsymbol{F}(t)$ is the electric field of the laser pulse, $\psi_i(\boldsymbol{r},t) = \psi_0(\boldsymbol{r})e^{iI_p t}$ is the bound-state wave function unperturbed by the laser field with I_p the ionization potential, and

$$\psi_{\boldsymbol{p}}(\boldsymbol{r},t) = \exp\left\{ i[\boldsymbol{p}+\boldsymbol{A}(t)]\cdot\boldsymbol{r} - \frac{i}{2}\int^{t} \left[\boldsymbol{p}+\boldsymbol{A}(t')\right]^2 dt' \right\} \tag{S2}$$

is the Volkov state (in the length gauge), where $\boldsymbol{A}(t)$ is the vector potential of the laser pulse. With a further saddle-point approximation [7, 8], tunneling exit characteristics can be extracted within the SFA framework. Here, the saddle-point equation (SPE) reads

$$\frac{1}{2}[\boldsymbol{p}+\boldsymbol{A}(t_s)]^2 + I_p = 0, \tag{S3}$$

where $t_s = t_r + it_i$ is a complex solution to the SPE, with t_r the tunneling exit time and t_i related to the ionization probability.

In the scenario of strong-field ionization, where the Keldysh parameter $\gamma \approx \omega t_i$ is small, we may expand the vector potential $\boldsymbol{A}(t_s)$ in terms of small t_i up to second order [3, 9–13]

$$\boldsymbol{A}(t_r + it_i) = \boldsymbol{A}(t_r) - it_i\boldsymbol{F}(t_r) + \frac{1}{2}t_i^2\dot{\boldsymbol{F}}(t_r) + O(t_i^3), \tag{S4}$$

where $\dot{\boldsymbol{F}}(t_r) = \frac{d\boldsymbol{F}(t_r)}{dt_r}$. Insertion of the expansion into the SPE [Eq. (S3)] results in

$$\boldsymbol{k}_\perp(t_r)\cdot\boldsymbol{F}(t_r) = 0, \tag{S5}$$

$$t_i = \sqrt{\frac{k_\perp^2(t_r) + 2I_p}{F^2(t_r) - \boldsymbol{k}_\perp(t_r)\cdot\dot{\boldsymbol{F}}(t_r)}}, \tag{S6}$$

where $\boldsymbol{k}_\perp(t_r) = \boldsymbol{p}_\perp + \boldsymbol{A}(t_r)$ is the transverse momentum at the tunnel exit with the $\perp$ subscript denoting variables in the polarization plane. The tunneling exit position can be obtained by

$$\boldsymbol{r}_0 = \mathrm{Re}\int_{t_s}^{t_r}[\boldsymbol{p}+\boldsymbol{A}(t)]dt = \mathrm{Im}\int_0^{t_i}\boldsymbol{A}(t_r+it)dt = -\frac{\boldsymbol{F}}{2}\frac{k_\perp^2+2I_p}{F^2-\boldsymbol{k}_\perp\cdot\dot{\boldsymbol{F}}}, \tag{S7}$$

and the angular momentum at the tunnel exit is subsequently obtained by

$$\boldsymbol{L} = \boldsymbol{r}_0 \times \boldsymbol{k}_\perp = \frac{F k_\perp}{2} \frac{k_\perp^2 + 2I_p}{F^2 - \boldsymbol{k}_\perp \cdot \dot{\boldsymbol{F}}} \boldsymbol{e}_z = \frac{k_\perp (k_\perp^2 + 2I_p)}{2(F + \tilde{\omega} k_\perp)} \boldsymbol{e}_z, \tag{S8}$$

where a slowly varying envelope approximation has been applied in the last step and

$$\tilde{\omega} = \frac{\varepsilon \omega}{\varepsilon^2 \cos^2(\omega t) + \sin^2(\omega t)}. \tag{S9}$$

The energy at the tunnel exit is

$$E = \frac{1}{2} k_\perp^2 + \boldsymbol{r}_0 \cdot \boldsymbol{F}(t) = \frac{1}{2} k_\perp^2 - \frac{F^2}{2} \frac{k_\perp^2 + 2I_p}{F^2 - \boldsymbol{k}_\perp \cdot \dot{\boldsymbol{F}}} = \frac{\tilde{\omega} k_\perp^3 - 2I_p F}{2(F + \tilde{\omega} k_\perp)} = \tilde{\omega} \frac{k_\perp (k_\perp^2 + 2I_p)}{2(F + \tilde{\omega} k_\perp)} - I_p = \tilde{\omega} L_z - I_p. \tag{S10}$$

Clearly, for the elliptical polarization, the subcycle conservation law is associated with different angular frequencies throughout the optical cycle, ranging from $\varepsilon\omega$ to ω/ε. For circular polarization where $\varepsilon = 1$, we have $\tilde{\omega} = \omega$, the above relation reduces to

$$E = \omega L_z - I_p, \tag{S11}$$

where the conservation law has a fixed angular frequency of ω, in coincident to the photon energy.

To assess the property of the conservation law at the subcycle level, we show the SAME at the tunnel exit at different time instances, see Figs. S1 and S2 corresponding to circular and elliptical light pulses, respectively. In the case of circular pulse as shown in Fig. S1, the SAME consistently adheres to the same circular conservation law [Eq. (S11)] at all time instances, even in the presence of pulse envelope. This indicates the applicability of the conservation law at the subcycle level. Interestingly, the conservation law possess an angular frequency that is identical to the normal photons. For elliptical pulse as shown in Fig. S2, the SAME follows straight lines as well, albeit with varying slope at different time instances. Close scrutiny reveals that the slope varies between $\varepsilon\omega$ and ω/ε, in agreement with the above theoretical formulations. When the electric field peaks, the slope is $\varepsilon\omega$; while when the electric field reaches minima, the slope becomes ω/ε. This points to the fact that the conservation law have different angular frequencies at different time instances within an optical cycle. Since tunneling ionization is a highly nonlinear process, the ionization rate is exponentially related to the electric field strength, the time-integrated SAME thus has roughly a slope of $\varepsilon\omega$.

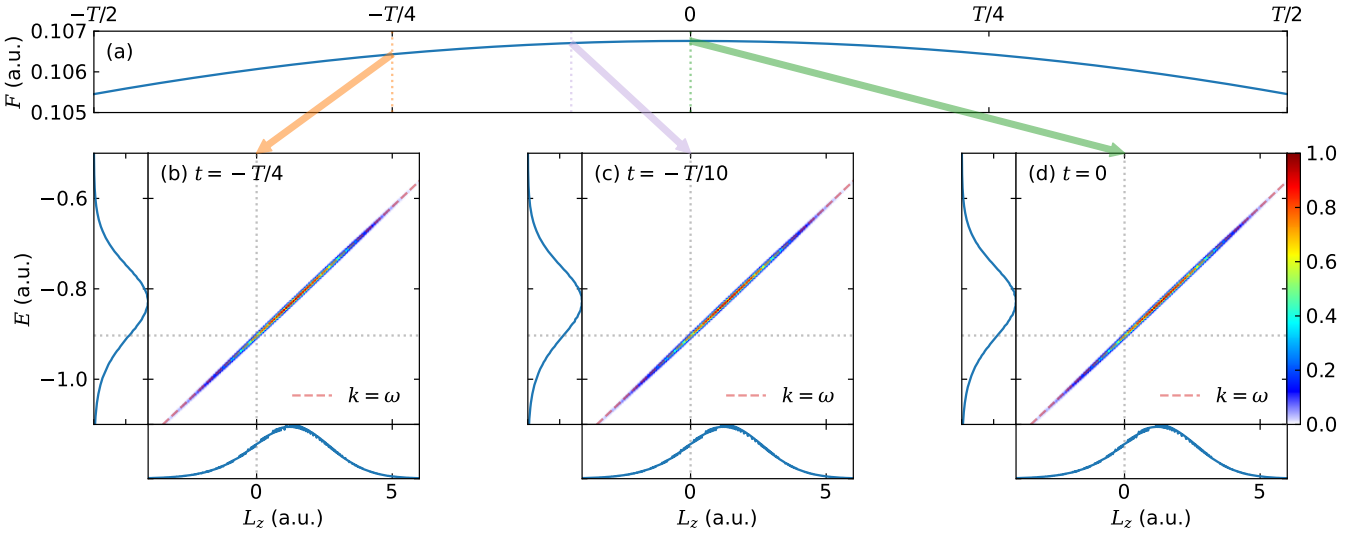

FIG. S1. (a) Total electric field magnitude F of a circularly polarized laser pulse. Refer to the main text for other laser parameters. (b-d) Correlation spectrum of angular momentum and energy (SAME) of photoelectrons at the tunnel exit ionized at different time instances. In panels (b-d), the left subfigure shows the distribution of energy, and the lower subfigure shows the distribution of angular momentum. The red dashed line denotes $E = \omega L_z - I_p$. Note that the color maps are normalized across different time instances.

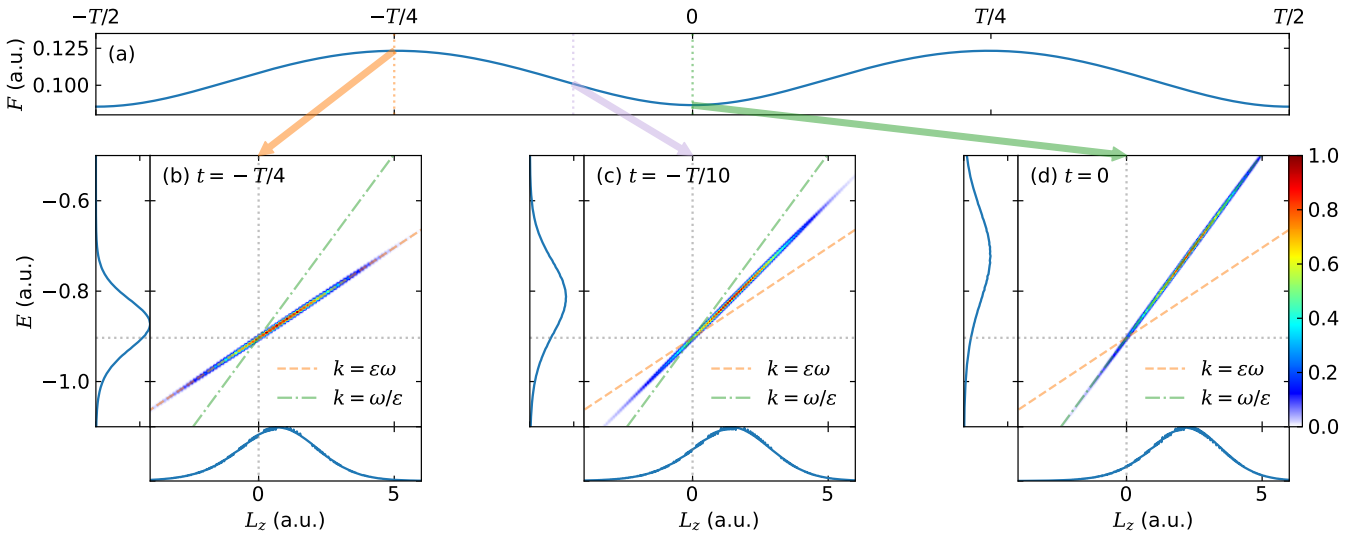

FIG. S2. (a) Total electric field magnitude F of an elliptically polarized laser pulse with ellipticity $\varepsilon = 0.7$. Refer to the main text for other laser parameters. (b-d) Correlation spectrum of angular momentum and energy (SAME) of photoelectrons at the tunnel exit ionized at different time instances. In panels (b-d), the left subfigure shows the distribution of energy, and the lower subfigure shows the distribution of angular momentum. The orange dashed line denotes $E = \varepsilon\omega L_z - I_p$ and the green dash-dotted line denotes $E = (\omega/\varepsilon)L_z - I_p$. Note that the color maps are normalized across different time instances.

S2. RELATIONSHIP BETWEEN ANGULAR FREQUENCY IN THE SUBCYCLE CONSERVATION LAW AND EFFECTIVE ANGULAR FREQUENCY OF THE LASER FIELD

The existence of the subcycle conservation law is reflected through the SAME of photoelectrons, revealing a conservation law governing the relationship between the angular momentum L_z and energy E. Under elliptically polarized laser pulses, the conservation law is expressed as $E = \tilde{\omega}L_z - I_p$, where $\tilde{\omega}$ is the angular frequency of the conservation law. Remarkably, this

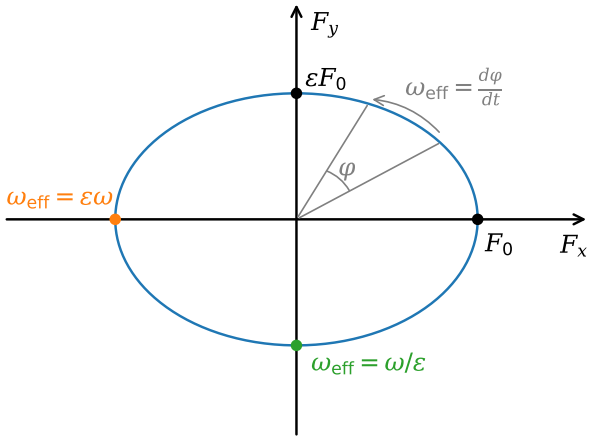

FIG. S3. Definition of effective angular frequency ω_{eff}. The blue line is the rotating electric field. The effective angular frequency at the field peak is $\varepsilon\omega$ (marked by the orange dot), and the effective angular frequency at the field valley is ω/ε (marked by the green dot).

angular frequency can be shown to correspond to the effective angular frequency $\omega_{\rm eff}$ of the laser field:

$$\omega_{\rm eff} = \frac{d\varphi}{dt} = \frac{d\arctan\left(F_y/F_x\right)}{dt} = \frac{\overbrace{d\arctan}^{\text{rotation}}\left[-\overbrace{\varepsilon}^{\text{squeezing/stretching}}/\tan(\omega t)\right]}{\underbrace{dt}_{\text{time translation}}} = \frac{\varepsilon\omega}{\varepsilon^2\cos^2(\omega t)+\sin^2(\omega t)} = \tilde{\omega}. \tag{S12}$$

Note that the pulse envelope cancels out here, and so this observation applies to short pulses as well. Obviously, for elliptical pulses, a squeezing or stretching operation is necessary before applying rotation, which is manifested as the ellipticity of the pulse in Eq. (S12), or the ratio of the magnitude of the electric field in the y to that in the x direction, as shown also in Fig. S3.

The infinite-order dynamical symmetry is related to the joint time translation and rotation operation, where the rotation angle $\delta\varphi$ within a small time interval δt follows $\delta\varphi = \omega_{\rm eff}\delta t$. The effective angular frequency thereby bridges these two operations. It applies to both circularly and elliptically polarized laser pulses with envelopes.

Under circularly polarized laser pulses, the effective angular frequency $\omega_{\rm eff}$ corresponds to the angular frequency ω of the laser field, essentially equating the angular frequency in the conservation law with that of the photon. Under elliptically polarized laser pulses, the effective angular frequency $\omega_{\rm eff}$ exhibits a time dependence, which in turn results in a time-varying angular frequency associated with the conservation law. Through the definition of effective angular frequency Eq. (S12), we can obtain $\omega_{\rm eff}(t)$ at different moments t within the elliptically polarized laser pulse. The results are shown in Fig. S3. When the laser field is at its peak (marked by the orange dot), the effective angular frequency is smaller than the angular frequency of the laser field, the electric field of the elliptically polarized laser pulses is stretched relative to the circularly polarized laser pulses. When the electric field is at its valley (marked by the green dot), the effective angular frequency is greater than the angular frequency of the laser field, the electric field of the elliptically polarized laser pulses is squeezed relative to the circularly polarized laser pulses.

Although the subcycle conservation law applies to elliptically polarized light pulses, there is a limited range of its applicability. In particular, the conservation law fails for near linear polarization. On the one hand, strong backscattering for near linear polarization would kill the generally isotropic photoelectron momentum distribution. On the other hand, in the limiting case of linear polarization, the rotation operation loses its meaning, where the angular frequency is a binary value of either 0 or ∞. Therefore, the applicability of the subcycle conservation law is limited to pulse with a sufficiently large ellipticity, say, $\varepsilon > 0.3$.

S3. PHASE RETRIEVAL AND SUBCYCLE CONSERVATION LAW IN THE ASYMPTOTIC REGION

To uncover the property of the subcycle conservation law in the asymptotic region, we need to construct the SAME from the asymptotic photoelectron momentum distribution. While energy is easily obtained from the momentum distribution, the evaluation of angular momentum is nontrivial since its information is encoded in the phase structure of the photoelectron momentum distribution. To retrieve the phase information, one would naturally consider to design an approach which brings together two exact replicas of the same original pattern where the phase information can be decoded from the interference pattern originating from the two replicas. This is exactly what we do here in this study. We employ two time-delayed counter-rotating circularly

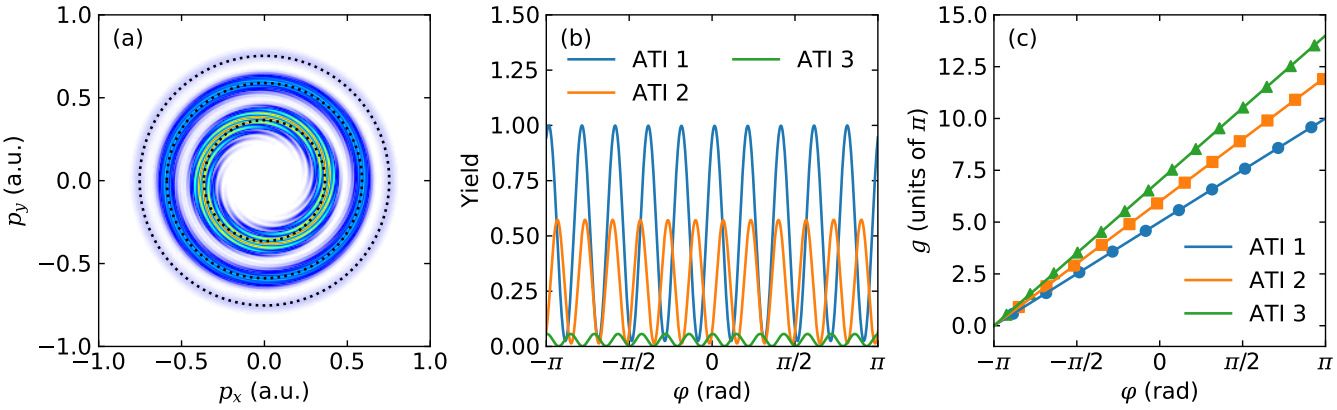

FIG. S4. (a) Photoelectron momentum distribution resulting from the ionization of hydrogen atoms by the time-delayed counter-rotating circularly polarized laser pulse after focal volume averaging. (b) Yield at different ATI orders corresponding to the black dotted line in panel (a). (c) Phase g extracted from the vortex structure.

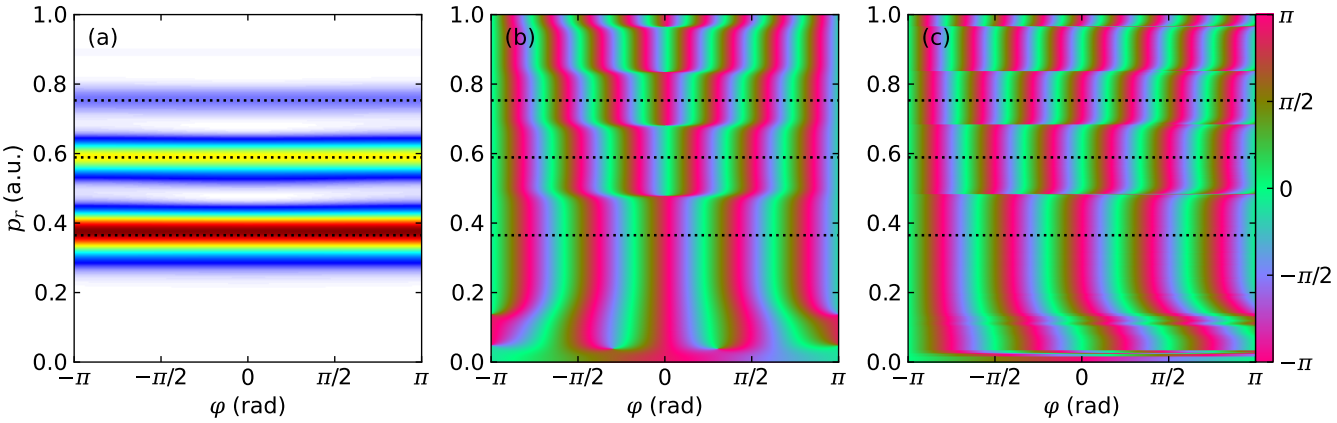

FIG. S5. (a) Momentum and (b) phase distribution of electron wave packets ionized by a circularly polarized laser pulse obtained by direct numerical evaluation of Eq. (S1). (c) Phase distribution extracted through the vortex structure. The distributions are shown in polar coordinate.

polarized light pulses to induce interferences in the photoelectron momentum distribution known as electron vortices [14–17], with the total field defined by

$$\boldsymbol{A}(t) = A_0 \cos^4\left(\frac{\omega t}{2N}\right)\begin{pmatrix}\cos(\omega t)\\ \sin(\omega t)\end{pmatrix} + A_0\cos^4\left[\frac{\omega(t-\tau)}{2N}\right]\begin{pmatrix}\cos[\omega(t-\tau)]\\ -\sin[\omega(t-\tau)]\end{pmatrix}, \tag{S13}$$

where τ is the time delay between the two circular pulses.

Shown in Fig. S4(a) is the photoelectron momentum distribution obtained using SFA resulting from the ionization of hydrogen atoms by the time-delayed counter-rotating circularly polarized pulse, where clear electron vortex structures are visible. Each individual circular pulse has a wavelength of 400 nm and an optical cycle number $N = 10$. The peak-to-peak time delay between the two pulses is $\tau = 11T$. In addition, we have performed focal volume averaging, where a total of 15 different intensities are calculated in the range of $I = 2.0 \sim 3.4 \times 10^{13}$ W/cm^2 and the results are summed with a weight given by $(I_0 + 2I)\sqrt{I_0 - I}/I^{5/2}$ [18, 19], where $I_0 = 3.4 \times 10^{13}$ W/cm^2 is the peak intensity.

To retrieve the phase information from the electron vortex structure, we write down the amplitude of ionization by one individual circular pulse as $M_p \propto R(p)\exp(ig(\varphi))$, where $R(p)$ is a real function of the electron momentum and $g(\varphi)$ stands for an angular phase distribution [20]. Thereby, the electron wave packet ionized by the two time-delayed counter-rotated circularly polarized laser pulses can be approximated as

$$\Psi = R(p)\exp(-iE_p\tau)\exp(ig(\varphi)) + R(p)\exp(iI_p\tau)\exp(-ig(\varphi)), \tag{S14}$$

where $E_p = p^2/2$. The vortex structure can then be expressed as

$$|\Psi|^2 = 2R(p)\left\{1 + \cos\left[(E_p + I_p)\tau - 2g(\varphi)\right]\right\}. \tag{S15}$$

Evidently, the angular distribution exhibits cosine oscillations at specific energies, see Fig. S4(b). At oscillation valleys, the phase $g(\varphi)$ satisfies $(E_p + I_p)\tau - 2g(\varphi) = (2n+1)\pi$ with $n \in \mathbb{Z}$. Hence, the phase of the electronic wave packet can be extracted from the minima of the oscillations. An additional fit to the phase $g(\varphi)$ leads to an well-defined expression of $g(\varphi)$, as shown in Fig. S4(c). Repeating the procedure for all energies, we can construct the momentum-resolved phase distribution, as shown in Fig. S5(c). In order to check the accuracy of the extracted phase, we directly calculate the momentum-resolved phase distribution by numerically evaluating Eq. (S1), and the resulting distribution is depicted in Fig. S5(b). Clearly, the retrieved phase distribution agrees well with direct numerical results, which means the present phase retrieval procedure is reliable. It is worth noting that the extracted phase is only accurate near the ATI peaks, as shown in Fig. S5(a), marked by the black dotted lines.

With the reliably retrieved phase distribution of the photoelectron momentum distribution, the angular momentum distribution in the asymptotic region can be obtained by applying the angular momentum operator $\hat{L}_z = -i\frac{\partial}{\partial\varphi}$ to the complex amplitude of photoelectron wave packet in the momentum space. The SAME in the asymptotic region can be subsequently constructed, as shown in Fig. 4(b) of the main text. Remarkably, the conservation law in the asymptotic region follows slightly differently from that at the tunnel exit in the form of

$$E = \omega L_z - I_p - U_p, \tag{S16}$$

with an additional ponderomotive term $-U_p$.

In order to pinpoint the physical origin of the change in the conservation law from the tunnel exit to the asymptotic region, we assume that the electron is ionized at time instant t_r and then moves in the remaining laser field $\boldsymbol{F}(t)$, ignoring the Coulomb interaction of the parent ion on the electron. The equation of motion is expressed as

$$\ddot{\boldsymbol{r}}(t) = -\boldsymbol{F}(t), \tag{S17}$$

the velocity of the electron can be written as

$$\boldsymbol{k}(t) = \boldsymbol{k}_0 - \int_{t_r}^{t} \boldsymbol{F}(t')dt' = \boldsymbol{k}_0 - \boldsymbol{A}(t_r) + \boldsymbol{A}(t), \tag{S18}$$

where $\boldsymbol{k}_0 = \boldsymbol{k}_\perp(t_r)$ is the initial velocity of the electron at the tunnel exit [Eq. (S5)], and the corresponding final velocity of the electron is

$$\boldsymbol{k}_f = \boldsymbol{k}_0 - \boldsymbol{A}(t_r) = \boldsymbol{k}_\perp(t_r) - \boldsymbol{A}(t_r). \tag{S19}$$

The position of the electron is

$$\boldsymbol{r} = \boldsymbol{r}_0 + \int_{t_r}^{t} \boldsymbol{k}(t')dt' = \boldsymbol{r}_0 + \int_{t_r}^{t} \left[\boldsymbol{k}_0 - \boldsymbol{A}(t_r) + \boldsymbol{A}(t')\right] dt' = \boldsymbol{r}_0 + \left[\boldsymbol{k}_0 - \boldsymbol{A}(t_r)\right](t - t_r) - \boldsymbol{R}(t_r) + \boldsymbol{R}(t), \tag{S20}$$

where $\boldsymbol{R}(t) = \int^t \boldsymbol{A}(t')dt'$ is the quiver representation of the laser field and $\boldsymbol{r}_0$ is the initial position at the tunnel exit [Eq. (S7)]. The final position of the electron is thus

$$\boldsymbol{r}_f = \boldsymbol{r}_0 + \left[\boldsymbol{k}_\perp(t_r) - \boldsymbol{A}(t_r)\right](t_f - t_r) - \boldsymbol{R}(t_r). \tag{S21}$$

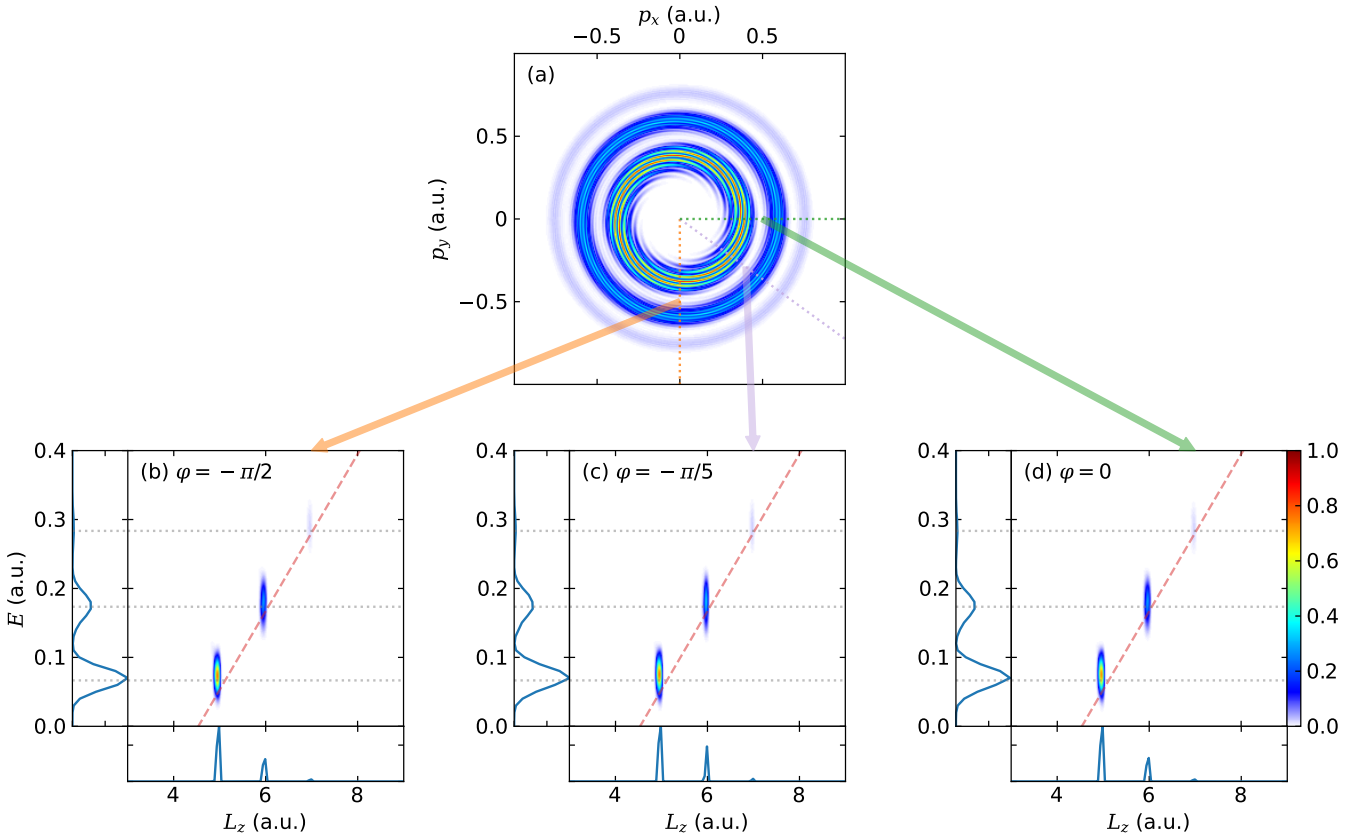

FIG. S6. (a) Photoelectron momentum distribution resulting from the ionization of hydrogen atoms by the time-delayed counter-rotating circularly polarized laser pulse after focal volume averaging. (b-d) Correlated spectrum of angular momentum and energy at different emission angles. The red dashed line denotes $E = \omega L_z - I_p - U_p$.

Therefore, the angular momentum of the electron at the end of the laser field is

$$\boldsymbol{L} = \boldsymbol{r}_f \times \boldsymbol{k}_f = \left\{\boldsymbol{r}_0 + [\boldsymbol{k}_\perp(t_r) - \boldsymbol{A}(t_r)](t_f - t_r) - \boldsymbol{R}(t_r)\right\} \times [\boldsymbol{k}_\perp(t_r) - \boldsymbol{A}(t_r)] = [\boldsymbol{r}_0 - \boldsymbol{R}(t_r)] \times [\boldsymbol{k}_\perp(t_r) - \boldsymbol{A}(t_r)]. \tag{S22}$$

For long circular pulses, we have

$$\boldsymbol{L} = \left(-\frac{\boldsymbol{F}}{2}\frac{k_\perp^2 + 2I_p}{F^2 - \boldsymbol{k}_\perp \cdot \dot{\boldsymbol{F}}} - \frac{\boldsymbol{F}}{\omega^2}\right) \times (\boldsymbol{k}_\perp - \boldsymbol{A}) = \left[\frac{k_\perp^2 + 2I_p}{2(F_0 + \omega k_\perp)} + \frac{A_0}{\omega}\right](k_\perp + A_0)\,\hat{\boldsymbol{e}}_z. \tag{S23}$$

The energy of the electron at the end of the laser field is

$$\begin{aligned} E &= \frac{1}{2}(k_\perp + A_0)^2 = \frac{1}{2}(k_\perp + A_0)^2 + \omega L_z - \omega L_z = \omega L_z - \left[\frac{\omega(k_\perp^2 + 2I_p)}{2(F_0 + \omega k_\perp)} + A_0\right](k_\perp + A_0) + \frac{1}{2}(k_\perp + A_0)^2 \\ &= \omega L_z - \left[\frac{\omega(k_\perp^2 + 2I_p)}{F_0 + \omega k_\perp} + A_0 - k_\perp\right]\frac{(k_\perp + A_0)}{2} = \omega L_z - \frac{\omega(A_0^2 + 2I_p)}{F_0 + \omega k_\perp}\frac{(k_\perp + A_0)}{2} = \omega L_z - I_p - U_p. \end{aligned} \tag{S24}$$

We proceed to investigate the property of the conservation law at the subcycle level, i.e., at different emission angles in the asymptotic region, see Fig. S6. Evidently, the SAME adheres to the same conservation law at different emission angles, or at different time instances within an optical cycle.

We stress that, unlike previous studies [20, 21], where *ad hoc* assumptions regarding the phase $g(\varphi)$ are made, our phase retrieval procedure is free from assumptions. Therefore, the present study provides unambiguous support for the existence of the conservation law at the subcycle level, both at the tunnel exit and in the asymptotic region.

S4. INFLUENCE OF COULOMB POTENTIAL

Comparing Figs. 2(a1) and 2(b1) of the main text, we find that the SAME in Fig. 2(b1), obtained from SFA, adheres closely to the conservation law [eq. (S11)], while that in Fig. 2(a1), obtained from backpropagation, has a slight downward offset and curvature with respect to the conservation law. Both effects are due to the influence of the Coulomb potential of the parent ion. To elucidate this point, we show in Fig. S7 a comparison of the SAME obtained from different methods, where Fig. S7(a) is obtained from backpropagation of the full helium single-active-electron potential [22]

$$V(r) = -\frac{Z_c + a_1 e^{-a_2 r} + a_3 r e^{-a_4 r} + a_5 e^{-a_6 r}}{r}, \tag{S25}$$

where $Z_c = 1.0$, $a_1 = 1.231$, $a_2 = 0.662$, $a_3 = -1.325$, $a_4 = 1.236$, $a_5 = -0.231$, $a_6 = 0.480$; Fig. S7(b) is obtained from backpropagation of a short-range potential of the form

$$V(r) = -\frac{e^{-100r} + e^{-r^2/2}}{\sqrt{r^2 + a}}, \tag{S26}$$

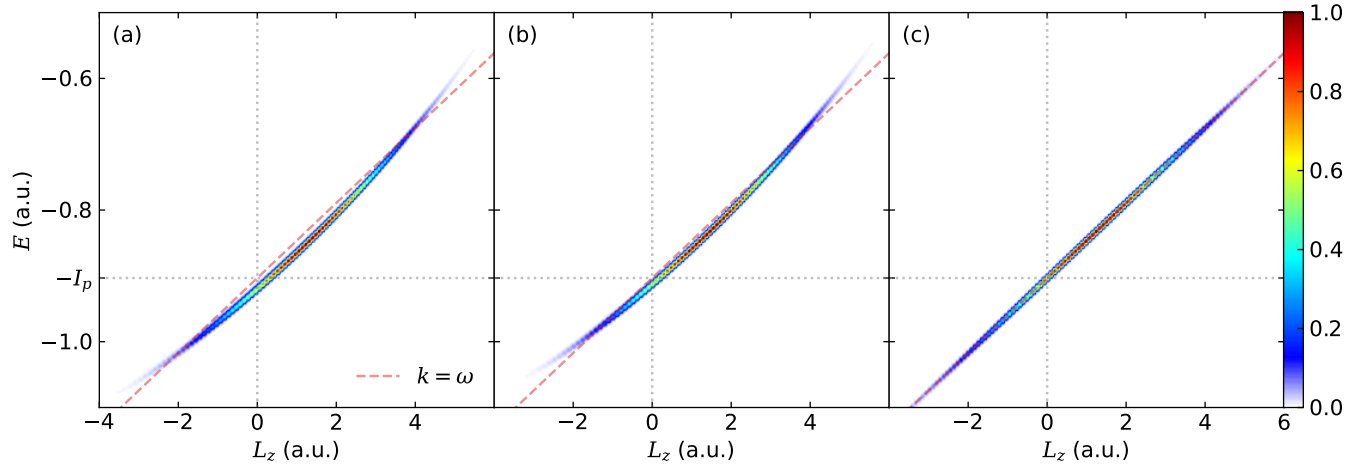

FIG. S7. Correlated spectrum of angular momentum and energy (SAME) of photoelectrons at the tunnel exit obtained from (a) backpropagation of the helium potential, (b) backpropagation of the short-range potential, and (c) SFA.

where the soft-core parameter a is tuned so that the ionization potential matches that of the helium atom; and Fig. S7(c) is obtained from SFA which takes full account of the pulse envelope. Comparing Figs. S7(a) and S7(b), it is clear that the offset is smaller for the short-range potential. Needless to say, the short-range potential still differs from a zero-range potential as in the case of SFA. That is why the SAME in Fig. S7(b) still has a small offset, while that from SFA as in Fig. S7(c) has zero offset. In addition, the SAME obtained from SFA in Fig. S7(c) fully accounts for the pulse envelope, so the curvature in Figs. S7(a) and S7(b) also arises from the influence of the Coulomb potential.

S5. TRAJECTORY ANALYSIS

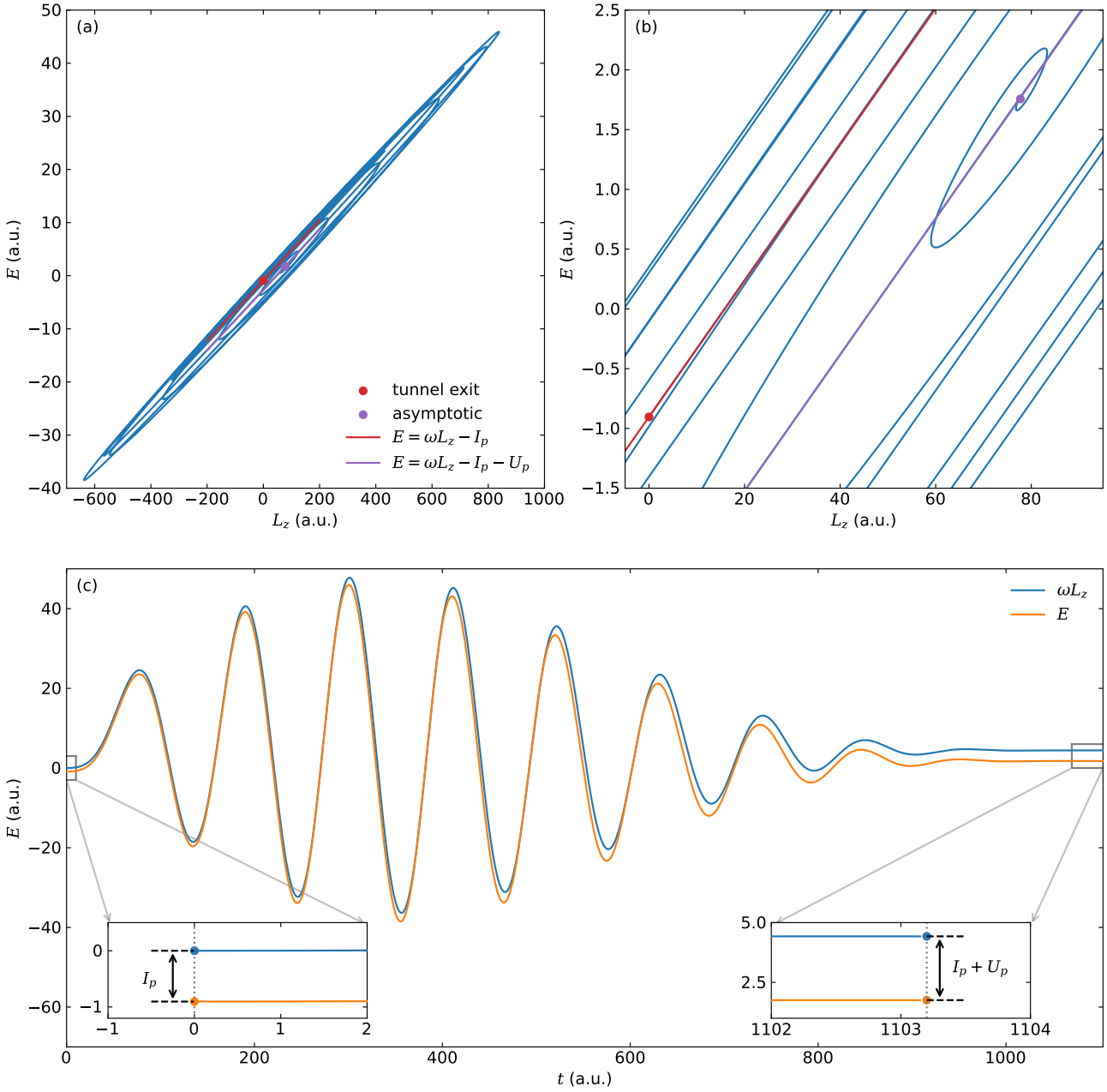

FIG. S8. (a) The angular momentum and energy of a typical electron trajectory during continuum motion in the laser field. (b) A zoomin of panel (a). (c) Evolution of the angular momentum ωL_z and energy E of the electron trajectory until the end of the laser field. The red dot and purple dot are the angular momentum and energy corresponding to the photoelectron at the tunnel exit and in the asymptotic region, respectively. The difference between the red line and the purple line is that their intercepts are different, while their slopes are both ω.

The conservation laws are different for at the tunnel exit and in the asymptotic region. For circular polarization, it is $E = \omega L_z - I_p$ at the tunnel exit, while it is $E = \omega L_z - I_p - U_p$ in the asymptotic region.

We employ a trajectory analysis to demonstrate how the relationship between the angular momentum and energy evolves after tunneling. To this end, we pick a typical electron trajectory, which is launched from the center of the pulse with a vanishing initial velocity, and monitor its angular momentum and energy during its continuum excursion in the absence of the Coulomb potential of the parent ion until it reaches the detector in the asymptotic region.

Shown in Fig. S8(a) is the SAME of this typical electron trajectory while Fig. S8(b) is its zoomin at a local region, and shown in Fig. S8(c) is the time evolution of ωL_z and E after electron release until the end of the laser pulse. Not surprisingly, the relationship between the angular momentum and energy satisfies $E = \omega L_z - I_p$ at the tunnel exit while it satisfies $E = \omega L_z - I_p - U_p$ in the asymptotic region. During its continuum excursion, interestingly, $\omega L_z - E$ gradually changes from I_p to $I_p + U_p$, and the respective relationship between ωL_z and E in the SAME stays essentially with a near-constant slope that is still close to ω (photon exchange during excursion), and the relationship gradually changes until reaching the detector in the asymptotic region.

S6. LEFT CIRCULAR POLARIZATION

For circular polarization, the main text has focused on right circular polarization with $\varepsilon = +1$. For left circular polarization with $\varepsilon = -1$, the conservation law changes to

$$E = -\omega L_z - I_p \tag{S27}$$

at the tunnel exit, as shown in Fig. S9. Therefore, a more universal expression for the conservation law under circular polarization would be

$$E = \mathrm{sgn}(\varepsilon)\omega L_z - I_p. \tag{S28}$$

We note that the conservation law in the case of elliptical polarization

$$E = \tilde{\omega}(t) L_z - I_p \tag{S29}$$

is universal and applicable to both right and left elliptical polarizations, since the effective angular frequency

$$\tilde{\omega}(t) = \frac{\varepsilon\omega}{\varepsilon^2 \cos^2(\omega t) + \sin^2(\omega t)} \tag{S30}$$

could be positive or negative, depending if the laser is right or left elliptically polarized. It also correctly reduces to Eq. (S28) for both right and left circular polarizations.

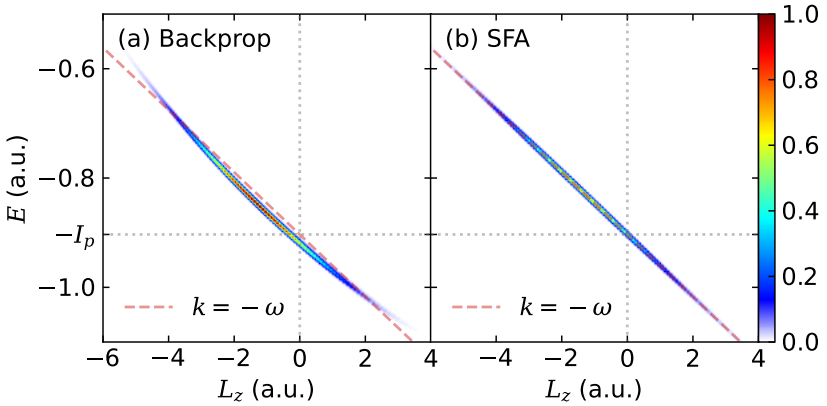

FIG. S9. Correlated spectrum of angular momentum and energy (SAME) at the tunnel exit for photoelectrons originating from ionization of the helium atom exposed to left circularly polarized laser pulses at a wavelength of 800 nm and a peak intensity of 8.0×10^{14} W/cm^2. Panel (a) presents the results obtained from backpropagation and panel (b) depicts the results of SFA. The slope is denoted by $k = -\omega$ (red dashed line).

[1] H. Ni, U. Saalmann, and J.-M. Rost, Tunneling ionization time resolved by backpropagation, Phys. Rev. Lett. **117**, 023002 (2016).

[2] H. Ni, U. Saalmann, and J.-M. Rost, Tunneling exit characteristics from classical backpropagation of an ionized electron wave packet, Phys. Rev. A **97**, 013426 (2018).

[3] H. Ni, N. Eicke, C. Ruiz, J. Cai, F. Oppermann, N. I. Shvetsov-Shilovski, and L.-W. Pi, Tunneling criteria and a nonadiabatic term for strong-field ionization, Phys. Rev. A **98**, 013411 (2018).

[4] C. Hofmann, A. Bray, W. Koch, H. Ni, and N. I. Shvetsov-Shilovski, Quantum battles in attoscience: tunnelling, Eur. Phys. J. D **75**, 208 (2021).

[5] S. V. Popruzhenko, J. Phys. B **47**, 204001 (2014).

[6] K. Amini, J. Biegert, F. Calegari, A. Chacón, M. F. Ciappina, A. Dauphin, D. K. Efimov, C. Figueira de Morisson Faria, K. Giergiel, P. Gniewek, A. S. Landsman, M. Lesiuk, M. Mandrysz, A. S. Maxwell, R. Moszyński, L. Ortmann, J. Antonio Pérez-Hernández, A. Picón, E. Pisanty, J. Prauzner-Bechcicki, K. Sacha, N. Suárez, A. Zaïr, J. Zakrzewski, and M. Lewenstein, Symphony on strong field approximation, Rep. Prog. Phys. **82**, 116001 (2019).

[7] A. Nayak, M. Dumergue, S. Kühn, S. Mondal, T. Csizmadia, N. Harshitha, M. Füle, M. Upadhyay Kahaly, B. Farkas, B. Major, V. Szaszkó-Bogár, P. Földi, S. Majorosi, N. Tsatrafyllis, E. Skantzakis, L. Neoričić, M. Shirozhan, G. Vampa, K. Varjú, P. Tzallas, G. Sansone, D. Charalambidis, and S. Kahaly, Saddle point approaches in strong field physics and generation of attosecond pulses, Phys. Rep. **833**, 1 (2019).

[8] A. Jašarević, E. Hasović, R. Kopold, W. Becker, and D. B. Milošević, Application of the saddle-point method to strong-laser-field ionization, J. Phys. A **53**, 125201 (2020).

[9] S. P. Goreslavski, G. G. Paulus, S. V. Popruzhenko, and N. I. Shvetsov-Shilovski, Coulomb asymmetry in above-threshold ionization, Phys. Rev. Lett. **93**, 233002 (2004).

[10] M. V. Frolov, N. L. Manakov, A. A. Minina, S. V. Popruzhenko, and A. F. Starace, Adiabatic-limit coulomb factors for photoelectron and high-order-harmonic spectra, Phys. Rev. A **96**, 023406 (2017).

[11] H. Ni, S. Brennecke, X. Gao, P.-L. He, S. Donsa, I. Březinová, F. He, J. Wu, M. Lein, X.-M. Tong, and J. Burgdörfer, Theory of subcycle linear momentum transfer in strong-field tunneling ionization, Phys. Rev. Lett. **125**, 073202 (2020).

[12] Y. Ma, J. Zhou, P. Lu, H. Ni, and J. Wu, Influence of nonadiabatic, nondipole and quantum effects on the attoclock signal, J. Phys. B **54**, 144001 (2021).

[13] X. Mao, H. Ni, X. Gong, J. Burgdörfer, and J. Wu, Subcycle-resolved strong-field tunneling ionization: Identification of magnetic dipole and electric quadrupole effects, Phys. Rev. A **106**, 063105 (2022).

[14] J. M. Ngoko Djiokap, S. X. Hu, L. B. Madsen, N. L. Manakov, A. V. Meremianin, and A. F. Starace, Electron vortices in photoionization by circularly polarized attosecond pulses, Phys. Rev. Lett. **115**, 113004 (2015).

[15] J. M. Ngoko Djiokap, A. V. Meremianin, N. L. Manakov, S. X. Hu, L. B. Madsen, and A. F. Starace, Multistart spiral electron vortices in ionization by circularly polarized uv pulses, Phys. Rev. A **94**, 013408 (2016).

[16] D. Pengel, S. Kerbstadt, D. Johannmeyer, L. Englert, T. Bayer, and M. Wollenhaupt, Electron vortices in femtosecond multiphoton ionization, Phys. Rev. Lett. **118**, 053003 (2017).

[17] D. Pengel, S. Kerbstadt, L. Englert, T. Bayer, and M. Wollenhaupt, Control of three-dimensional electron vortices from femtosecond multiphoton ionization, Phys. Rev. A **96**, 043426 (2017).

[18] S. Augst, D. D. Meyerhofer, D. Strickland, and S. L. Chin, Laser ionization of noble gases by coulomb-barrier suppression, J. Opt. Soc. Am. B **8**, 858 (1991).

[19] M.-M. Liu, M. Li, C. Wu, Q. Gong, A. Staudte, and Y. Liu, Phase structure of strong-field tunneling wave packets from molecules, Phys. Rev. Lett. **116**, 163004 (2016).

[20] X.-R. Xiao, M.-X. Wang, H. Liang, Q. Gong, and L.-Y. Peng, Proposal for measuring electron displacement induced by a short laser pulse, Phys. Rev. Lett. **122**, 053201 (2019).

[21] Y.-N. Qin, M. Li, Y. Feng, S. Luo, Y. Zhou, and P. Lu, Extracting the phase distribution of the electron wave packet ionized by an elliptically polarized laser pulse, Front. Phys. **16**, 1 (2021).

[22] X. M. Tong and C. D. Lin, Empirical formula for static field ionization rates of atoms and molecules by lasers in the barrier-suppression regime, J. Phys. B **38**, 2593 (2005).